Stiffness of a recycled composite aggregate

H. He[1], K. Senetakis[2], M.R. Coop[3]

[1] University of New South Wales (UNSW), Sydney Australia
[2] City University of Hong Kong, Hong Kong
[3] University College London, London, UK

Abstract

Recycled concrete aggregate (RCA) is a promising substitute for natural aggregates and the reuse of this demolished material would benefit the construction projects both economically and environmentally. A difficulty associated with the prediction of the behavior of RCA is because of its multi-composition which is linked to the grain size in consideration. In this study, a comprehensive laboratory testing program is conducted on different fractions of RCA for which the ratio of silicon over calcium increases for the coarser fractions due to the limitation of the cement mortar inclusion as the mean size increases. The study incorporates bender/extender element tests capturing small-strain constrained moduli, Young's moduli and Poisson's ratio of RCA fractions with different mean grain size and grain size distribution. For the uniform RCA fractions, the results showed that during isotropic compression, the specimens had a clear dependency of their dynamic properties on mean grain size. For the better graded specimens, it was shown that their behavior was dominated to some extend by the finer fraction they were composed rather than being affected equally by the different fractions they consisted of. The results also highlighted the sensitivity of the behavior of the samples to the over-consolidation stress history. For RCA, a multi-composition material, the grain size has a dominant role on the modulus – pressure relationship as well as the

sensitivity of material behavior to stress history and these observations must be considered in the analysis of geo-structures where RCA is used as construction material.

1. Introduction

The amount of concrete aggregate recycled from demolished buildings or structures has risen rapidly in recent years (e.g. Poon and Chan 2007). Facing the increasing need of aggregates in engineering construction and the rising cost of natural aggregates, recycled concrete aggregate (RCA) has become a promising and economic substitution. Benefitting from extensive research on RCA, the material is starting to be used as a non-structural construction element in practical projects, including geotechnical engineering and pavement geotechnics applications (e.g. Rilem Recommendation, 1994, Sagoe-Crentsil et al., 1996, Hansen, 2004, Poon and Chan, 2007, Rahardjo et al., 2013, Tatsuoka et al., 2013, He and Senetakis, 2016a, 2016b). This replacement of the natural aggregates releases, partly, the pressure from both the demand of quarry sites and the cost of land-fill disposal.

In modeling the behavior of RCA when used as a geotechnical material, stiffness at small strains is a key property. Material small-strain stiffness is a critical parameter for the prediction of the deformations of geo-structures and soil-structure interaction problems. The stiffness of geo-materials, including the shear modulus (G), constrained modulus (M) and Young's modulus (E), reaches its maximum value in the elastic range of behavior (generally less than 10^{-3}% strain). The bender element test (BE) (Shirley and Anderson, 1975), which is a high-frequency dynamic testing technique that uses a pair of piezo-element inserts, is widely adopted to capture the shear wave velocity (V_s) for the purpose of deriving the small-strain soil shear modulus (G_{max}) (e.g. Viggiani and Atkinson, 1995, Jovicic et al., 1996, Lee

and Santamarina, 2005, Youn et al., 2008, Leong et al., 2009, Alvarado and Coop, 2012, Airey and Mohsin, Gu et al., 2013). The same pair of bender elements can also be configured to send primary waves (P-waves) and measure their propagation velocity (V_p), denoted as extender element mode (EE) (used by Lings and Greening, 2001, Leong et al., 2009, Kumar and Madhusudhan, 2010a, 2010b, He and Senetakis, 2016b, among others). The small-strain constrained modulus (M_{max}), Young's modulus (E_{max}) and Poisson's ratio (ν) can be thereafter derived from the knowledge of V_s, V_p and the specimen density, thus the complete characterization of the small-strain behavior of geo-materials can be implemented based on measurements from bender/extender element tests.

In the light of examining in this study sand-sized recycled concrete aggregate, particular focus has been paid on the associated literature on granular materials. Based on published works on the dynamic properties of sand-sized materials, it can be concluded that the major properties that affect their dynamic behavior at small strains at a given isotropic confining pressure are the void ratio, the coefficient of uniformity, the particle shape and overall morphology as well as the mineral composition (e.g. Hardin and Richart, 1963, Chung et al., 1984, Cascante and Santamarina, 1996, Jovicic and Coop, 1997, Santamarina et al., 2001, Menq, 2003, Cho et al., 2006, Wichtmann and Triantafyllidis, 2009, 2010, Senetakis et al., 2012, Payan et al., 2016, 2017, among others). Although work on other materials, for example natural sands of single mineralogy or reference granular materials such as glass beads, has not reported any significant effect on G_{max} when changing the mean grain size of the material (e.g. Menq, 2003, Wichtmann and Triantafyllidis, 2009, Senetakis et al., 2012, Yang and Gu, 2013), a recent study on recycled concrete aggregate by He and Senetakis (2016a) reported a clear dependency of the sensitivity of G_{max} to pressure on the mean grain size (D_{50}), which sensitivity must be captured for accurate predictions of geo-structures

deformations (Clayton, 2011). He and Senetakis (2016b) conducted a characterization of the material through consolidated-drained triaxial shearing tests, breakage analysis after one-dimensional compression tests and the shear and primary wave velocities as well as the Poisson's ratio (ν) measurements of two fractions of RCA, 0.60-1.18 mm and 1.18-2.36 mm. That study highlighted the significant stress history influence on the dynamic properties of the aforementioned fractions. He and Senetakis (2016b) also reported on the small to medium strain stiffness degradation and damping characteristics throughout the conduction of resonant column tests. Although He and Senetakis (2016b) reported on the shear and Young's moduli of RCA, that study focused only on two uniform fractions, while in another study, He and Senetakis (2016a) investigated the effect of mean grain size on G_{max}, covering a wide range of sizes but of uniform fractions with no information for constrained modulus, Young's modulus and Poisson's ratio which would be necessary to capture completely the small-strain properties of RCA.

For the complete modeling of the small-strain behavior of geo-materials, it is necessary to quantify, apart from the shear modulus, the constrained modulus or Young's modulus as well as the Poisson's ratio. However, in the literature, there has been a relatively limited amount of work examining both shear and primary wave velocities (or shear and Young's modulus) as well as material Poisson's ratio of sands (e.g. Saxena and Reddy, 1989, Kumar and Madhusudhan, 2010a, Wichtmann and Triantafyllidis, 2010, Chen et al., 2016, Payan et al., 2017). Even though in many research works and practical applications, Poisson's ratio is considered as a constant, recent laboratory works have highlighted that Poisson's ratio (ν) is notably affected by the effective confining pressure in the range of small strains, while, Kumar and Madhusudhan (2010a) found an additional effect of material porosity. An effort to explain the micromechanics behind the pressure dependency of Poisson's ratio was

presented in their study by Gu et al. (2013) through numerical simulations. Given that the Poisson's ratio is affected by the confining pressure, the necessity of the knowledge of both shear and Young's moduli of the material is stressed.

In this study, the constrained modulus, Young's modulus and Poisson's ratio of a range of uniform fractions (from 0.15-0.30 mm to 2.36-4.75 mm) and poorly graded recycled concrete aggregate (RCA) specimens are investigated with a set of bender/extender element tests. The small-strain constants of different uniform fractions were measured and compared through an array of dynamic tests to study whether there is an effect of mean grain size on the dynamic behavior of the RCA, particularly in correlating the different small-strain properties (i.e. constrained modulus and Poisson's ratio) with the size and size distribution of RCA grains. This is particularly important for this type of geo-material since SEM-EDS analysis from He and Senetakis (2016a) has shown that RCA is a multi-compositional material and this composition varies with the fraction (i.e. grain size). The Young's modulus constants during the isotropic swelling stages are also examined for a limited number of specimens. In practice, it is possible that RCA will be used in a relatively better graded form rather than a single size fraction. Thus, apart from the study of uniform fractions of RCA, which provides some fundamental insights into the behavior of those complex materials, additional experiments on better graded specimens (denoted in the study as poorly graded samples) were conducted to study the effect of grading. Thus, the major contributions of this work are:

(i) The complete characterization of the small-strain properties of RCA fractions providing some insights into the role of their multi-compositional nature (exploring constraint modulus, Young's modulus and Poisson's ratio). A detailed analysis of the loading and unloading small-strain constants and the comparison with a Young's modulus literature model are given;

(ii) Compare the dynamic properties of the poorly graded RCA specimens with the uniform fractions and explain the different observed trends from a fundamental point of view;

(iii) Provide empirical expressions, based on the experiments, to correlate small-strain properties to important factors (e.g. pressure and grain size) which comprise simple but useful tools in modeling the behavior of geo-materials. This could provide practical but also some theoretical aspects of the dynamic behavior of recycled concrete aggregate with many potential applications in geotechnical engineering.

2. Materials and methods

2.1 Material properties

The recycled concrete aggregate tested in the current study was demolished, crushed and supplied by an Australian supplier (New South Wales). After the crushing process, the recycled concrete consisted of a well-graded aggregate which includes gravel, sand and silt sized grains. Therefore, sieving was conducted before testing and sand sized aggregates are focused on in this study. Five uniform fractions (with coefficient of uniformity, $C_u \approx 1.4$) together with three better graded materials, denoted as poorly-graded fractions ($C_u \approx 2.8$), which are mixtures of three successive single fractions, were studied and the grading curves for all the materials are given in Figure 1. The particle sizes of the uniform samples are 0.15-0.30 mm (denoted as RCA02), 0.30-0.60 mm (denoted as RCA03), 0.60-1.18 mm (denoted as RCA04), 1.18-2.36 mm (denoted as RCA05) and 2.36-4.75 mm (RCA06), respectively. The samples with higher C_u were produced by evenly mixing three successive fractions. For example, RCA234 consisted of RCA02, RCA03 and RCA04, with each uniform fraction

taking up 33.3% of the total. The mixing process increased the C_u, while keeping the D_{50} of the middle fraction unchanged.

The uniform fractions were classified through their mean grain size, specific gravity of solids (G_s), particle shape and mineral composition. The specific gravity values, which are given in Table 1, were tested adopting the ASTM standard (ASTM, 2000). The particle shape parameters for different fractions were estimated by visual observation through an optical microscope and images taken from a Scanning Electron Microscope (SEM). An image of the parent concrete aggregate and a representative SEM photo of the RCA05 are given in Figures 2 and 3, respectively. An empirical chart proposed by Krumbein and Sloss (1963) was used as reference to quantify the particle shape characteristics through visual comparison with the particles and achieve both the sphericity (S) and roundness (R) measurements. The method is a well-established, even though empirical, quantification approach to describe the shape of granular materials. The arithmetic average value of the S and R gives the regularity (ρ) of the particle (Cho et al., 2006). At least 30 particles were examined by two operators for each fraction and the mean values and the standard deviations (SDV) of the regularities for the uniform fractions are presented in Figure 4 (after He and Senetakis, 2016a). Within the scatter of the data, it is observed that ρ decreased from 0.60 to 0.40 from the finest (RCA02) to the coarsest (RCA06) fractions.

Except for the presence of minor amount of silty material and bricks, the recycled concrete aggregate is mostly composed of aggregate and cement mortar. From previous studies, it has been reported that the percentage of cement mortar increases as the aggregate mean grain size decreases (Tam and Tam, 2007). As the dynamic properties of the soil, particularly the modulus – pressure relationship, are closely related to the mineralogy (Cascante and Santamarina, 1996, Jovicic and Coop, 1997, Santamarina et al., 2001, Senetakis et al., 2012),

the percentage of the aggregate and cement mortar in different fractions is a key parameter. To measure the percentage of different components of the RCA, a set of Scanning Electronic Microscope-Energy Dispersive Spectroscopy (EDS) tests was performed on a pure cement specimen, four specimens from four different uniform fractions (RCA02, RCA03, RCA05 and RCA06) and a poorly graded specimen (RCA234). The EDS analysis is an effective and accurate way to identify, map and quantify the elements in specimens. He and Senetakis (2016a) conducted EDS analysis of the uniform RCA fractions. Through their EDS results, it is shown that among a variety of elements, the most abundant in the RCA specimens are calcium (Ca), silicon (Si) and oxygen (O) (the amount of carbon (C) could not be captured because the specimens were carbon coated prior to the tests to increase their conductivity). Since the cement mortar is mostly composed of calcium compounds, while the natural aggregates are predominantly silicon compounds, the Ca/Si ratio is used as an indication of the composition. The measured Ca/Si ratios for some representative fractions, one pure cement specimen, together with one better graded specimen (RCA234) are presented in Figure 5 (updated after He and Senetakis, 2016a). It was found that the calcium to silicon ratio appeared to decrease as the mean grain size of the uniform fractions increases and this ratio was the highest for the pure cement specimen. As expected, the RCA234 specimen gave a value close to that of the RCA03 (of similar mean grain size). The decrease of the ratio Ca/Si indicated that the relative amount of cement mortar content decreases gradually and the coarser fractions are composed mostly of aggregate.

2.2Dynamic experimental methods

A fixed-free type of Stokoe resonant column system with bender/extender element inserts implemented was used to conduct dynamic tests under different isotropic confining pressures. As is illustrated in Figure 6, the resonant column system houses a specimen with dimensions

of 10 cm in height and 5 cm in diameter. The resonant column was used to apply a range of isotropic pressures to the specimens from 50 to 800 kPa. On both the top cap and the pedestal, a piezo-element insert is located, which is capable of generating both shear waves (S-waves) and primary waves (P-waves). When configured to bender element (BE) mode, one of the piezo-inserts triggers shear waves (S-waves) and the other acts as receiver, while in extender element (EE) mode, the role of sender and receiver are exchanged to generate and receive primary waves (P-waves) (Lings and Greening, 2001). The shear wave velocity (V_s) or primary wave velocity (V_p) is then calculated from the recorded wave propagation time and the distance between the tips of the inserts. Thereafter, the small-strain constrained modulus (M_{max}) and Poisson's ratio (ν) can be calculated using Eq. (1) and (2), where ρ_s is the mass density of the soil specimen.

$$M_{\max} = \rho_s \times V_p^2 \tag{1}$$

$$\nu = \frac{0.5 \times V_p^2 - V_s^2}{V_p^2 - V_s^2} \tag{2}$$

From the knowledge of M_{max} and ν, the small-strain Young's modulus could be derived from the following equation:

$$E_{\max} = \frac{M_{\max} \times (1+\nu) \times (1-2\times\nu)}{(1-\nu)} \tag{3}$$

2.3 Testing program

All the specimens were constructed in a metal split mold in 3 layers of similar heights. The dry air-pluviation technique was adopted to prepare loose specimens with high initial void ratios (e_o). For medium dense to dense specimens, a light-weight rod was used to compact the specimens in layers achieving higher relative density. Before removing the mold, a small vacuum (≈5 kPa) was applied to hold the specimen. Then, the dimensions of the specimen

were measured and recorded under the suction for the calculation of the initial void ratio (e_o). The testing program of the uniform fraction specimens is given in Table 1, while the testing series for the poorly graded specimens is listed in Table 2. All the specimens were loaded isotropically in progressive stages. BE and EE tests were conducted at 50 kPa, 100 kPa, 200 kPa, 400 kPa, 600 kPa (if applicable) and 800 kPa (if applicable), after which, dynamic tests were also conducted on some of the uniform fraction specimens during the isotropic swelling stage (details are given in Table 1). The maximum pressure each specimen reached was 400 kPa, 600 kPa or 800 kPa.

3. Tests results and analysis

3.1 Extender element signal analysis and M_{max}-p' relationship

Both the first arrival and peak to peak methods were performed to estimate the primary wave (P-wave) propagation time and a representative signal analysis from one of the specimens is given in Figure 7. The input signal had a voltage amplitude of 14V and the received signal waves were amplified 500 times to be distinguishable. Similar to the work by Kumar and Madhusudhan (2010b), both the first arrival and peak to peak methods gave satisfactorily close values for all the tests (maximum error $\leq$ 10%) but the first arrival method was adopted for further analysis. For the shear wave velocities, the average of the first arrival and peak to peak values were adopted as explained by He and Senetakis (2016b). This interpretation method of the shear wave velocity was validated by the satisfactory comparison between the bender element and the resonant column test results by He and Senetakis (2016b). A comparison of V_s and V_p measurements between the two different methods used is given in Figure 8.

Based on Eq. (1), with the measured V_p and the density of the specimen, the small-strain constrained modulus M_{max} can be calculated. Since the RCA specimens are isotropically loaded, when plotting the normalized M_{max} against normalized mean effective stress p' the data follow a power-law type of the general expression (given in Eq. (4)) that is widely adopted in soil dynamics research:

$$M_{\max} / f(e) = (A_M) \times \left(\frac{p'}{1kPa} \right)^{n_M} \quad (4)$$

$$f(e) = e^{-1.3} \quad (5)$$

where A_M is material constant and n_M is a power that depicts the sensitivity of the stiffness to pressure. The f(e) is a void ratio function (given in Eq. (5)) used to eliminate the density effect in the analysis (after Jamiolkowski et al., 1991) and the mean effective stress is divided by 1kPa to remove the unit. Note that since the specimens are isotropically consolidated, p' = $\sigma'_a = \sigma'_r$, where σ'_a and σ'_r correspond to the effective axial and effective radial stresses, respectively.

Typical plots of normalized M_{max} versus mean effective stress (p') from two representative specimens and their best fitting power-law equations are given in Figure 9. All the tests were analyzed in a similar way to Figure 9, and a summary of the results from the tests on the uniform RCA fractions, in terms of the constrained modulus constants A_M and n_M are plotted against the mean grain size D_{50} is given in Figure 10. As is shown on Figure 10(a), there is a very clear trend that A_M increases as the mean grain size increases. Based on a power-law best fitting curve of the A_M-D_{50} plot (Figure 10(a)), the power is found to be 0.44. Despite some scatter of the finest fraction RCA02 (0.15-0.30 mm), the trend is quite clear with a coefficient of determination (R^2) of 0.88.

Similarly, the power n_M is plotted against D_{50} in Figure 10(b) for all the specimens. The power values decrease as D_{50} increases. For RCA02, the n_M values are between 0.49-0.54, while those for RCA06 are in the range of 0.34-0.35. This drop is quite drastic as the average power value dropped about 33% from the finest to the coarsest fraction. The power law best fitting of the n_M-D_{50} curve gives a power value of -0.15 and the R^2 value is equal to 0.93.

He and Senetakis (2016a) found a decrease of n_G values as particle size increases, though much smaller in magnitude, but they did not report any systematic effect of particle size on the small-strain constant A_G values. Yang and Gu (2013) studied the small-strain shear modulus of a reference material (i.e. glass beads) of three different grain sizes (D_{50}). Through their analysis, both experimental and micromechanical, it was found that the variation of the shear modulus between specimens constructed of different mean particle sizes was negligible. Therefore, the trends of increasing A_M and decreasing n_M of the RCA specimens with the increase of grain size should be attributed, predominantly, to the change of the composition of the RCA fractions. This is because the stiffness – pressure relationship of granular materials is affected markedly by the grain contact response which in turn is affected by the material of the surfaces in contact (Cascante and Santamarina, 1996, Santamarina et al., 2001, Senetakis and Madhusudhan, 2015). For smaller sizes of RCA, there is an increase of cement-cement and cement-aggregate contacts since the content of cement mortar increases. This gives rise to a more pronounced plastic-to-brittle in nature contact response which is believed to contribute to the trends shown in Figure 10. This is because the nature of particle contact response has a dominant effect on the modulus – pressure relationship, expressed through the power n_M in Figure 10(b) (Cascante and Santamarina, 1996).

3.2E_{max}-p' relationships

Like M_{max}, the small-strain Young's modulus (E_{max}) can also be fitted by a power law general formula, which is given in the following equation.

$$E_{\max} / f(e) = (A_E) \times \left(\frac{p'}{1kPa} \right)^{n_E} \quad (6)$$

where A_E and n_E are the Young's modulus constants and the void ratio function f(e) is given in Eq. (5). From a previous study, Payan et al. (2017) proposed a model for E_{max} prediction based on a set of tests on quartz sands with a range of particle regularities (ρ) and coefficients of uniformity (C_u). Based on their tests, the proposed general model is given as follows,

$$E_{\max} = \left(245 C_u^{-0.09} \times \rho^{0.82} \right) \times e^{-1.32} \times \left(\frac{p'}{p_a} \right)^{\left(C_u^{0.11}\right)(-0.44\rho+0.66)} \quad (7)$$

where C_u is the coefficient of uniformity of the specimen, ρ is the particle shape regularity, e is the void ratio of the specimen at the corresponding pressure stage and p_a is the atmospheric pressure (100kPa). The formula was used to predict the Young's modulus of the RCA specimens and the comparison between the predicted and measured results is given in Figure 11. The measured and predicted E_{max} against the mean effective stress p' from two representative specimens are plotted in Figure 11(a). It is found that for the RCA particle shapes and grading characteristics, the Young's modulus values are predicted to be much smaller than the measured ones. In Figure 11(b), the maximum error of the stiffness prediction is about 50% compared to the measured values. In a previous study of the RCA G_{max}, He and Senetakis (2016a) have also reported underestimation of the small-strain shear modulus from the general formula proposed by Payan et al. (2016) based on quartz sands. The failure of the prediction in both cases is believed to be due to two reasons. Firstly, similar

to the volcanic sands studied by Senetakis et al. (2012) and (2016), the RCA is a material with intra-particle voids due to the presence of cement mortar, which leads to higher void ratio and lower dry density specimens compared to typical quartz sand specimens that are composed of massive grains. Payan et al. (2016, 2017) proposed models for G_{max} and E_{max} based on experiments on quartz sands that had no intra-particle voids, so only inter-particle voids were considered when calculating the void ratio values. Consequently, as the void ratio is elevated by the intra-particle voids, the E_{max} prediction would be lowered. Secondly, the particle surface of the RCA is always coated with a cement layer, which can be observed from the close view of the SEM images. The cement layer is expected to be much softer and more plastic in nature compared to quartz sand surfaces. Therefore, the stiffness sensitivity to pressure is also expected to be higher (Cascante and Santamarina, 1996, Senetakis and Madhusudhan, 2015).

Thereafter, when plotting the constants A_E and n_E versus D_{50} (Figure 12), quite similar trends to the A_M and n_M against D_{50} plots were observed as A_E increases while n_E decreases as the mean grain size increases. When fitted to the power law, the following relationships for A_E and n_E with D_{50} are found,

$$A_E = 18.8\left(D_{50}\right)^{0.23} \tag{8}$$

$$n_E = 0.51\left(D_{50}\right)^{-0.07} \tag{9}$$

The coefficient of determination R^2 values for the power fitting in Figures 12(a) and (b) are equal to 0.69 and 0.89, respectively. In terms of small-strain Young's modulus, the constants do not vary as much as the A_M and n_M values. The average power value n_E for each uniform fraction only dropped from 0.56 to 0.48 from RCA02 (D_{50}=0.21mm) to RCA06 (D_{50}=2.59mm).

The trends of the constants indicate that the coarser fractions exhibited higher Young's moduli in the lower pressure range, but they were less sensitive to pressure increments compared to the finer fractions. From the previous study by He and Senetakis (2016a), a similar drop of the small-strain shear modulus (G_{max}) power n_G, when D_{50} increased, was found. However, unlike the A_E or A_M, they reported no specific trend for the A_G values of different mean grain size uniform fractions.

3.3 ν-p' relationships

The Poisson's ratio of the specimens can be calculated from Eq. (2) with the knowledge of both V_s and V_p. The ν-p' relationship can be fitted with a power law type equation as follows,

$$\nu = A_\nu \times \left(\frac{p'}{1kPa} \right)^{n_\nu} \tag{10}$$

where A_ν and n_ν are the Poisson's ratio constants of the material. In agreement with previous works on granular soils (Nakagawa et al., 1996, Kumar and Madhusudhan, 2010a, Wichtmann and Triantafyllidis, 2010, Chen et al., 2016) as well as the previous study on two of the fractions of RCA (He and Senetakis, 2016b), the power n_ν is negative value for the specimens tested as the Poisson ratio decreased with the increase of the mean effective stress. The Poisson's ratio of the RCA specimens ranged between 0.30-0.37 at 25 kPa confining pressure and decreased to 0.25-0.30 at 800 kPa confining pressure. There was no effect of density on the constants A_ν and n_ν observed from any of the fractions tested, which is in accordance to the observations by Wichtmann and Triantafyllidis (2010) and He and Senetakis (2016b).

To illustrate the effect of D_{50} on the Poisson ratio, the mean absolute values of A_v and n_v and their standard deviations are plotted against the mean grain size for different uniform fraction specimens in Figure 13. No monotonic trend was observed from the data points and the constants for the coarser fractions were more scattered.

3.4Isotropic swelling E_{max}-p' relationships

One to three specimens from each fraction were tested during both isotropic loading (compression) and unloading (swelling) stages (Table 1). Similar to the previous observations of V_p measurements for RCA04 and RCA05 by He and Senetakis (2016b) and small-strain moduli of carbonate sand with crushable grains during the unloading stages by Jovicic and Coop (1997) and He et al. (2017), the small-strain Young's modulus was increased during the unloading stages compared to the corresponding stress level (p') in the loading stages. The loading and unloading normalized E_{max} behavior of one representative specimen (RCA03-3) is plotted as an example in Figure 14. The increase of the stiffness in the unloading stages would result in a higher unloading A_E value (equal to 49.1 MPa) and a lower unloading n_E value (equal to 0.33) compared to the loading process constants (A_E=11.1 MPa, n_E=0.55), which indicates that the sensitivity of the stiffness to pressure (slope of modulus-pressure relationship curve) is reduced after the material experiences a stress history. The comparison of the loading and unloading power value n_E for all the tests is given in Figure 15. Although there is a small scatter in the limited number of unloading power values, it is shown that during unloading, all the fractions are exhibiting a quite similar level of sensitivity to the stress change, or similar n_E values (around 0.34). The effect of the stress history is believed to be attributed to different factors including the rearrangement of the grains, the plastic-to-brittle contact response and the small amount of particle breakage during the isotropic compression stage (Cascante and Santamarina, 1996, He and Senetakis, 2016b).

For the purpose of comparing the magnitude of the effect of stress history between different fractions, the ratio between the unloading and the loading constant is calculated for each test and plotted against D_{50} in Figure 16. From the limited number of tests, it is shown that both ratios of (unloading A_E/loading A_E) and (unloading n_E/loading n_E) values for the finer fractions deviate more from unity than those for coarser fractions. The finer fractions are therefore more affected than the coarser ones in terms of modulus change from the loading (compression) to the unloading (swelling) stage.

3.5 Effect of C_u on E_{max} constants

The RCA used for engineering projects may have a better grading. Therefore, this study extended the analysis of the stiffness - pressure relationship to a set of RCA fractions with increased coefficient of uniformity and compared to the results from the tests on uniform fractions (mainly discussed in Section 3.2) to examine the effect of C_u on E_{max}. Three soils (RCA234, RCA345 and RCA456, respectively), each consisting of three consecutive uniform fractions, were tested with bender/extender element tests under several progressively increased isotropic stress stages (Table 2). Thereafter, similar to the uniform fraction tests, the Young's modulus was derived, normalized and fitted with the power law equation given in Eq. (6).

Figure 17(a) provides the A_E constant for each individual test against its D_{50}, including both the uniform fractions (Table 1) and the poorly graded specimens (Table 2). Through the comparison, despite the small scatter, at the same mean grain size level, it is observed clearly that the better-graded materials have lower small-strain constant (A_E) than the uniform ones. In order to quantify the effect of C_u on the constant A_E, Figure 17(b) shows the average A_E versus D_{50} for materials with different gradings but same mean grain size (D_{50}). From the

limited number of specimens tested at $C_u \approx 2.8$, the decrements of the A_E are quite clear and significant (23%, 23% and 11% for materials with D_{50}=0.42, 0.84 and 1.67 mm, respectively) as the coefficient of uniformity (C_u) increased from 1.4 (uniform fractions specimens) to 2.8 (poorly graded specimens). From the previous study on quartz sands, Payan et al. (2017) noticed that the increase of C_u would result in a decrease of the A_E constant, however, this effect was found to be less pronounced for quartz sands than the results on the RCA fractions of this study. From their empirical equation (Eq. (7)), when C_u is increased from 1.4 to 2.8, the A_E constant of the quartz sand would be predicted to drop about 6.0%. The notable drop of the A_E value for the RCA fractions is believed to be mainly due to the component of the finest fraction in the mixture of the RCA fractions. For the uniform RCA specimens, it was found that the finer fractions had lower A_E constant values, which means that the stiffness of the material is lower in comparison to the coarser fractions. From the data analysis (Figure 17(a)), it can be observed that despite a small scatter, the mixture of a fine fraction with two successive coarser fractions gave A_E values close to the uniform fine fraction level, which is lower than those for the coarser fractions included. When the soil contains a certain amount of softer (or weaker) material, the contact response is more likely to be dominated to some degree by the softest component, which is also found by the previous studies on soil-rubber mixtures composed of soft rubber grains and stiff sand grains (e.g. Feng and Sutter, 2000, Anastasiadis et al., 2012). In sand-rubber mixtures, which comprise as extreme example from the point of view of different properties between the two dominant elements (i.e. rubber and sand grains), the surface contact behavior is changed drastically compared to the pure sand, since the granulated rubber can be considered as highly deformable with nearly no stiffness in the small-strain range. Consequently, the wave propagation velocity is significantly reduced by the rubber thus reducing the stiffness of the mixture. For the RCA mixed fractions of the

present study, the inclusion of 33% of softer fine fraction materials (i.e. increased cement mortar component) would lower the general stiffness of the mixture drastically.

In terms of the power constant n_E, no specific trend was observed when changing the grading of the recycled concrete aggregate (as shown in Figure 18). Through the current set of tests, the sensitivity of the different gradings but same mean grain size materials appeared to be quite similar as shown in both Figures 18(a) and (b). The power n_E of the poorly graded specimens displayed a decreasing trend as the mean grain size increases, which is identical to what was observed in the uniform fraction tests. With the individual data points scattered in the same range between both materials in Figure 18(a), the average n_E values of two grading materials are close as is plotted in Figure 18(b). However, Payan et al. (2017) found a drop of the power while increasing the coefficient of uniformity. According to their empirical equation in Eq. (7), an increase of C_u from 1.4 to 2.8 would result in a drop of n_E of about 7.9%, which was not observed for the RCA tests.

4. Conclusions

The small-strain constrained modulus (M_{max}), Young's modulus (E_{max}) and Poisson's ratio (ν) of a recycled concrete aggregate (RCA) were examined in this study. The different fractions of RCA were characterized by their particle size, specific gravity, and composition using the Energy Dispersive Spectroscopy (EDS) technique. Through a set of bender and extender element tests, the dynamic properties of a set of uniform fraction specimens and an array of poorly graded specimens were measured and analyzed. The small-strain Young's modulus values of the uniform fraction specimens are compared with predicted values from an existing empirical equation and the comparison was found to be not satisfactory, with the

prediction underestimating the stiffness of the RCA. It appeared that both the small-strain constrained modulus and small-strain Young's modulus of the RCA are quite sensitive to the particle mean grain size. The stiffness constants A_M and A_E increased, while the power values n_M and n_E decreased, as the mean grain size (D_{50}) increased. This phenomenon is primarily attributed to the different ratios of cement and aggregate in the different fractions. As for the Poisson's ratio (ν), there was not observed any monotonic trend of the constants as the grain size changed. After the maximum pressure had been reached, some of the specimens were tested during isotropic swelling stages. The sensitivity to confinement change of the RCA specimens became smaller during isotropic swelling compared to isotropic compression. For finer fractions, the Young's modulus constants were altered more by the stress history than those of the coarser ones, which means the higher percentage of cement mortar in the finer fractions also resulted in a higher sensitivity to stress history. When testing RCA specimens with a higher coefficient of uniformity (C_u), a clear drop of the small-strain constants A_E was observed compared to uniform fraction specimens with the same mean grain size. The presence of the finer fraction may have softened the particle contact response, which led to this drop. On the other hand, the power n_E values of the same mean grain size remained the same when C_u increased.

Reference

Alvarado, G. & Coop, M. R. (2012) On the performance of bender elements in triaxial tests. *Géotechnique* 62(1):1-17.

Anastasiadis, A., Senetakis, K. & Pitilakis, K. (2012) Small-strain shear modulus and damping ratio of sand-rubber and gravel-rubber mixtures. *Geotechnical and Geological Engineering* 30(2):363-382.

ASTM D845 (2000) 854-00 Standard test method for specific gravity of soil solids by water pycnometer. *American Society for Testing and Materials. Annual book of ASTM Standards* 4:02.

Cascante, G. & Santamarina, J. C. (1996) Interparticle contact behavior and wave propagation. *Journal of Geotechnical Engineering* 122(10):831-839.

Chen, G., Zhou, Z., Pan, H., Sun, T. & Li, X. (2016) The influence of undrained cyclic loading patterns and consolidation states on the deformation features of saturated fine sand over a wide strain range. *Engineering Geology* 204:77-93.

Cho, G.-C., Dodds, J. & Santamarina, J. C. (2006) Particle shape effects on packing density, stiffness, and strength: Natural and crushed sands. *Journal of Geotechnical and Geoenvironmental Engineering* 132(5):591-602.

Chung, R. M., Yokel, F. Y. & Drnevich, V. (1984) Evaluation of dynamic properties of sands by resonant column testing. *Geotechnical testing journal* 7(2):60-69.

Feng, Z. & Sutter, K. (2000) Dynamic properties of granulated rubber/sand mixtures. *Geotechnical testing journal* 23(3):338-344.

Gu, X., Yang, J. & Huang, M. (2013) Laboratory measurements of small strain properties of dry sands by bender element. *Soils and Foundations* 53(5):735-745.

Hansen, T. C. (2004) *Recycling of demolished concrete and masonry*. CRC Press.

Hardin, B. & Richart, F. (1963) Elastic wave velocities in granular soils. *Journal of Soil Mechanics & Foundations Div* 89(SM1)(Proc. Paper 3407):33-65.

He, H. & Senetakis, K. (2016a) The effect of grain size on g max of a demolished structural concrete: A study through energy dispersive spectroscopy analysis and dynamic element testing. *Soil Dynamics and Earthquake Engineering* 89:208-218.

He, H. & Senetakis, K. (2016b) A study of wave velocities and poisson ratio of recycled concrete aggregate. *Soils and Foundations* 56(4):593-607.

He, H., Senetakis, K. & Ranjith, P. (2017) The behavior of a carbonate sand subjected to a wide strain range of medium-frequency flexural excitation. *Geomechanics and Geophysics for Geo-Energy and Geo-Resources* 3(1):51-60.

Jamiolkowski, M., Leroueil, S. & Lo Presti, D. (1991) Design parameters from theory to practice. In: Proceedings of the international conference on geotechnical engineering for coastal development. In *Geo-Coast 1991*, Coastal Development Institute of Technology, Yokohama, Japan, pp. 877-917.

Jovicic, V. & Coop, M. R. (1997) Stiffness of coarse-grained soils at small strains. *Géotechnique* 47(3):545-561.

Jovicic, V., Coop, M. R. & Simic, M. (1996) Objective criteria for determining gmax from bender element tests. *Géotechnique* 46(2):357-362.

Krumbein, W. C. & Sloss, L. L. (1963) *Stratigraphy and sedimentation. 2nd ed.*, W. H Freeman and Company.

Kumar, J. & Madhusudhan, B. N. (2010a) Effect of relative density and confining pressure on poisson ratio from bender and extender elements tests. *Géotechnique* 60(7):561-567.

Kumar, J. & Madhusudhan, B. N. (2010b) A note on the measurement of travel times using bender and extender elements. *Soil Dynamics and Earthquake Engineering* 30(7):630-634.

Ladd, R. (1978) Preparing test specimens using undercompaction. *Geotechnical testing journal* 1(1):16-23.

Lee, J.-S. & Santamarina, J. C. (2005) Bender elements: Performance and signal interpretation. *Journal of Geotechnical and Geoenvironmental Engineering* 131(9):1063-1070.

Leong, E. C., Cahyadi, J. & Rahardjo, H. (2009) Measuring shear and compression wave velocities of soil using bender-extender elements. *Canadian Geotechnical Journal* 46(7):792-812.

Lings, M. & Greening, P. (2001) A novel bender/extender element for soil testing. *Géotechnique* 51(8):713-717.

Menq, F.-Y. (2003) Dynamic properties of sandy and gravelly soils.) University of Texas at Austin, USA.

Nakagawa, K., Soga, K. & Mitchell, J. K. (1996) Pulse transmission system for measuring wave propagation in soils. *Journal of Geotechnical Engineering* 122(4):302-308.

Payan, M., Khoshghalb, A., Senetakis, K. & Khalili, N. (2016) Effect of particle shape and validity of Gmax models for sand: A critical review and a new expression. *Computers and Geotechnics* 72:28-41.

Payan, M., Senetakis, K., Khoshghalb, A. & Khalili, N. (2017) Effect of gradation and particle shape on small-strain young's modulus and poisson's ratio of sands. *International Journal of Geomechanics* 17(5).

Poon, C.-S. & Chan, D. (2007) The use of recycled aggregate in concrete in hong kong. *Resources, Conservation and Recycling* 50(3):293-305.

Rahardjo, H., Satyanaga, A., Leong, E.-C. & Wang, J.-Y. (2013) Unsaturated properties of recycled concrete aggregate and reclaimed asphalt pavement. *Engineering Geology* 161:44-54.

Rilem Recommendation (1994) Specifications for concrete with recycled aggregates. *Materials and Structures* 27(173):557.

Sagoe-Crentsil, K. K., Brown, T., Mak, S. L. & Taylor, A. (1996) Engineering properties and performance of concrete made with recycled construction aggregates. In *National Symposium on the Use of Recycled Materials in Engineering Construction: 1996; Programme & Proceedings*.) Institution of Engineers, Australia, pp. 132.

Santamarina, C., Klein, K. & Fam, M. (2001) *Soils and waves.* New York, John Wiley and Sons.

Saxena, S. K. & Reddy, K. R. (1989) Dynamic moduli and damping ratios for monterey no. 0 sand by resonant column tests. *Soils and Foundations* 29(2):37-51.

Senetakis, K., Anastasiadis, A. & Pitilakis, K. (2012) The small-strain shear modulus and damping ratio of quartz and volcanic sands. *Geotechnical testing journal* 35(6):964-980.

Senetakis, K. & Madhusudhan, B. N. (2015) Dynamics of potential fill–backfill material at very small strains. *Soils and Foundations* 55(5):1196-1210.

Senetakis K., Madhusudhan B.N., Anastasiadis A., (2016). Wave propagation attenuation and threshold strains of fully saturated soils with intra-particle voids. *Journal of Materials in Civil Engineering* ASCE, 28(2), 04015108.

Shirley, D. J. & Anderson, A. L. (1975) In situ measurement of marine sediment acoustical properties during coring in deep water. *IEEE Transactions on Geoscience Electronics* 13(4):163-169.

Tam, V. W. Y. & Tam, C. M. (2007) Crushed aggregate production from centralized combined and individual waste sources in hong kong. *Construction and Building Materials* 21(4):879-886.

Tatsuoka, F., Tomita, Y.-I., Iguchi, Y. & Hirakawa, D. (2013) Strength and stiffness of compacted crushed concrete aggregate. *Soils and Foundations* 53(6):835-852.

Viggiani, G. & Atkinson, J. (1995) Stiffness of fine-grained soil at very small strains. *Géotechnique* 45(2):249-265.

Wichtmann, T. & Triantafyllidis, T. (2009) Influence of the grain-size distribution curve of quartz sand on the small strain shear modulus gmax. *Journal of Geotechnical and Geoenvironmental Engineering* 135(10):1404-1418.
Wichtmann, T. & Triantafyllidis, T. (2010) On the influence of the grain size distribution curve on p-wave velocity, constrained elastic modulus m max and poisson's ratio of quartz sands. *Soil Dynamics and Earthquake Engineering* 30(8):757-766.
Yang, J. & Gu, X. (2013) Shear stiffness of granular material at small strains: Does it depend on grain size? *Géotechnique* 63(2):165.
Youn, J.-U., Choo, Y.-W. & Kim, D.-S. (2008) Measurement of small-strain shear modulus gmax of dry and saturated sands by bender element, resonant column, and torsional shear tests. *Canadian Geotechnical Journal* 45(10):1426-1438.

List of tables

Table 1 Dynamic testing program on single fraction (C_u=1.4) dry RCA specimens

Table 2 Dynamic testing program on poorly graded (C_u=2.8) dry RCA specimens

List of figures

Figure 1 Grading curves of recycled concrete aggregate (RCA) specimens tested: (a) uniform fractions (C_u≈1.4) (b) poorly graded fractions (C_u≈2.8)

Figure 2 Image of the parent concrete aggregate material (maximum grain size between 10 and 20 mm)

Figure 3 Scanning Electron Microscope (SEM) image of RCA05 (1.18-2.36 mm) fraction

Figure 4 Particle shape regularity mean values ± one standard deviation (He and Senetakis, 2016a)

Figure 5 EDS testing results: Calcium to Silicon ratio for pure cement, different uniform fractions of RCA and one poorly graded RCA (updated after He and Senetakis, 2016a)

Figure 6 The schematic plot of the Stokoe-type resonant and the dimensions of the specimen

Figure 7 Example of the signal analysis methods for extender element test (specimen RCA05-1) Note: the amplitude for the source wave was at 14 V while the received wave was magnified 500 times to be discernible in the same plot

Figure 8 Comparison between wave velocities (V_s and V_p) results derived from first arrival and peak to peak methods during bender/extender element tests

Figure 9 Typical plot of normalized constrained modulus (M_{max}) against mean effective stress (p') from two representative specimens: RCA06-1 and RCA03-2

Figure 10 Illustration of the effect of mean grain size (D50) on the small-strain constrained modulus constants: (a) Small-strain constant A_M and (b) Power n_M

Figure 11 Comparison between model predicted and measured small-strain Young's modulus values using the expression proposed by Payan et al. (2017): (a) measured E_{max} and predicted E_{max} against pressure from two representative tests; (b) all the measured and predicted Young's moduli

Figure 12 Illustration of the effect of mean grain size (D_{50}) on the small-strain Young's modulus constants: (a) Small-strain constants A_E versus D_{50} and (b) Power n_E against D_{50}

Figure 13 Illustration of the mean value ± one standard deviation for Poisson's ratio constants versus the mean grain size (D_{50}) from uniform fraction specimens: (a) Constants A_v versus D_{50} and (b) Power n_v against D_{50} (n_v are shown as absolute values)

Figure 14 Loading and unloading behavior of normalized small-strain Young's modulus $E_{max}/f(e)$ against mean effective stress p' (from specimen RCA03-3)

Figure 15 The comparison between loading and unloading power constant n_E

Figure 16 Unloading over loading small-strain Young's modulus constants versus mean grain size (D_{50}): (a) Unloading A_E/loading A_E against D_{50}; (b) Unloading n_E/loading n_E against D_{50}

Figure 17 Comparisons of the effect of mean grain size (D_{50}) on the small-strain Young's modulus constants between well graded (C_u=2.8) and single fractions (C_u=1.4) of RCA: (a) small-strain constants A_E versus D_{50} for each single test and (b) average A_E against D_{50}

Figure 18 Comparisons of the effect of mean grain size (D_{50}) on the small-strain Young's modulus constants between well graded (C_u=2.8) and single fractions (C_u=1.4): (a) small-strain constants n_E versus D_{50} for each single test and (b) average n_E against D_{50}

Table 1 Dynamic testing program on single fraction (C_u=1.4) dry RCA specimens

No.	Specimen code	Fraction (mm)	Mean grain size D_{50} (mm)	Specific gravity (G_s)	Preparation method	Loading Path	Max p' (kPa)	Initial void ratio e_o	Initial unit weight γ_{do} (kN/m^3)
1	RCA02-1	0.15-0.30	0.21	2.62	Air-pluviation	Loading	400	1.384	10.78
2	RCA02-2	0.15-0.30	0.21	2.62	Compaction	Loading	600	1.274	11.30
3	RCA02-3	0.15-0.30	0.21	2.62	Air-pluviation	Loading-Unloading	800	1.368	10.85
4	RCA02-4	0.15-0.30	0.21	2.62	Compaction	Loading-Unloading	800	1.190	11.72
5	RCA02-5	0.15-0.30	0.21	2.62	Compaction	Loading-Unloading	800	1.347	10.94
6	RCA03-1	0.30-0.60	0.42	2.48	Air-pluviation	Loading	600	0.934	12.58
7	RCA03-2	0.30-0.60	0.42	2.48	Compaction	Loading	600	1.056	11.83
8	RCA03-3	0.30-0.60	0.42	2.48	Compaction	Loading-Unloading	800	1.054	11.83
9	RCA04-1	0.60-1.18	0.84	2.47	Air-pluviation	Loading	400	1.264	10.70
10	RCA04-2	0.60-1.18	0.84	2.47	Compaction	Loading-Unloading	800	1.175	11.14
11	RCA04-3	0.60-1.18	0.84	2.47	Compaction	Loading	400	1.136	11.34
13	RCA05-1	1.18-2.36	1.67	2.47	Compaction	Loading-Unloading	600	1.233	10.85
14	RCA05-2	1.18-2.36	1.67	2.47	Compaction	Loading	800	1.200	11.01
15	RCA05-3	1.18-2.36	1.67	2.47	Compaction	Loading	600	1.248	10.78
16	RCA05-4	1.18-2.36	1.67	2.47	Compaction	Loading	400	1.183	11.09
17	RCA06-1	2.36-4.75	2.59	2.59	Air-pluviation	Loading-Unloading	400	1.255	11.27
18	RCA06-2	2.36-4.75	2.59	2.59	Compaction	Loading-Unloading	800	1.214	11.48

Table 2 Dynamic testing program on poorly graded (C_u=2.8) dry RCA specimens

No.	Specimen code	Fraction (mm)	Preparation method	Max p' (kPa)	e_o	γ_{do} (kN/m3)
1	RCA234-1	0.15-1.18	Compaction	800	0.895	13.30
2	RCA234-2	0.15-1.18	Compaction	800	1.002	12.35
3	RCA234-3	0.15-1.18	Air-pluviation	800	1.086	11.86
4	RCA345-1	0.30-2.36	Compaction	800	0.888	12.84
5	RCA345-2	0.30-2.36	Compaction	800	0.991	12.17
6	RCA345-3	0.30-2.36	Air-pluviation	800	1.090	11.59
7	RCA456-1	0.60-4.75	Compaction	800	1.000	12.30
8	RCA456-2	0.60-4.75	Compaction	400	1.039	12.06
9	RCA456-3	0.60-4.75	Air-pluviation	400	1.118	11.61

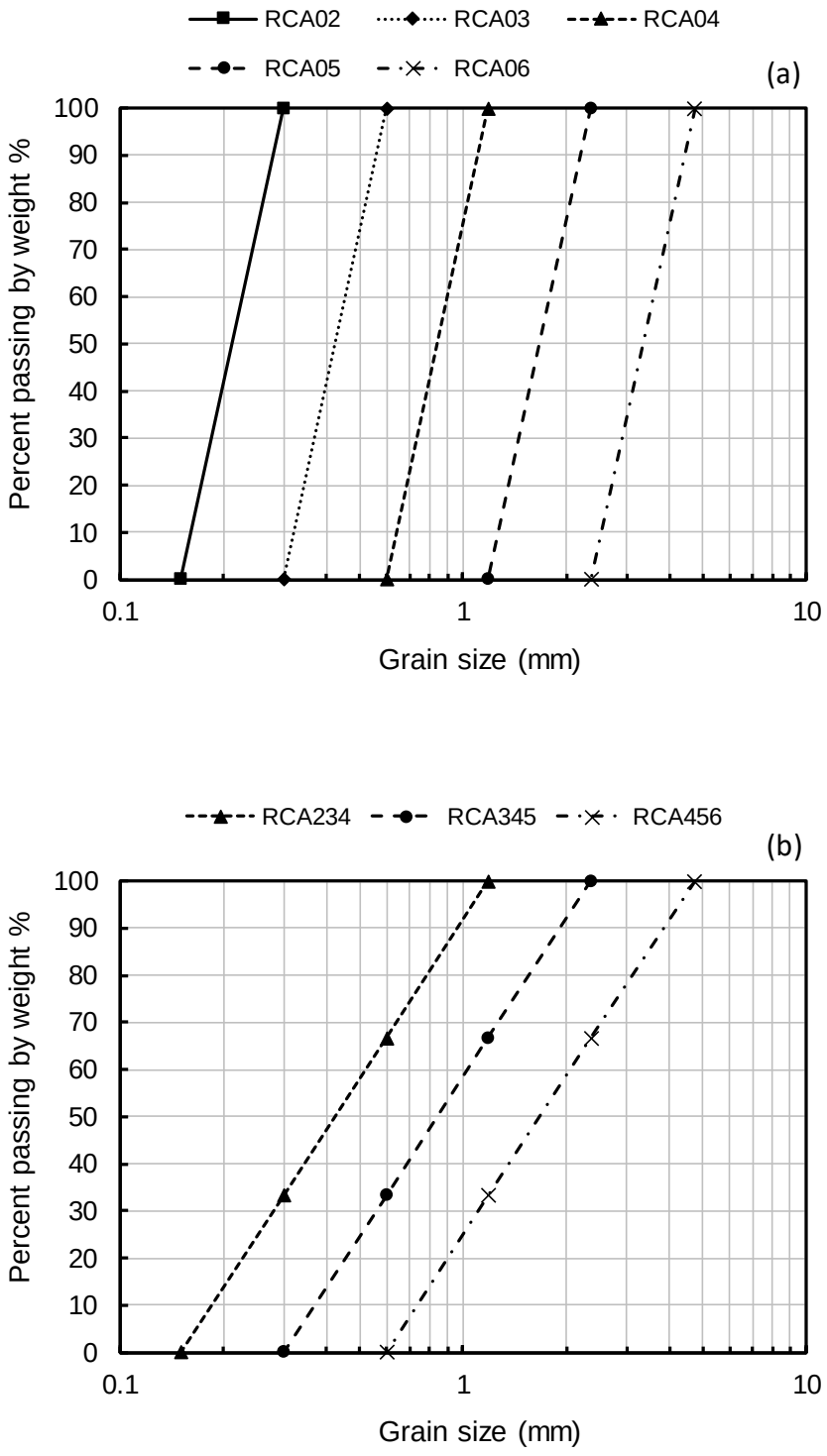

Figure 1 Grading curves of recycled concrete aggregate (RCA) specimens tested: (a) uniform fractions ($C_u \approx 1.4$) (b) poorly graded fractions ($C_u \approx 2.8$)

Figure 2 Image of the parent concrete aggregate material (maximum grain size between 10 and 20 mm)

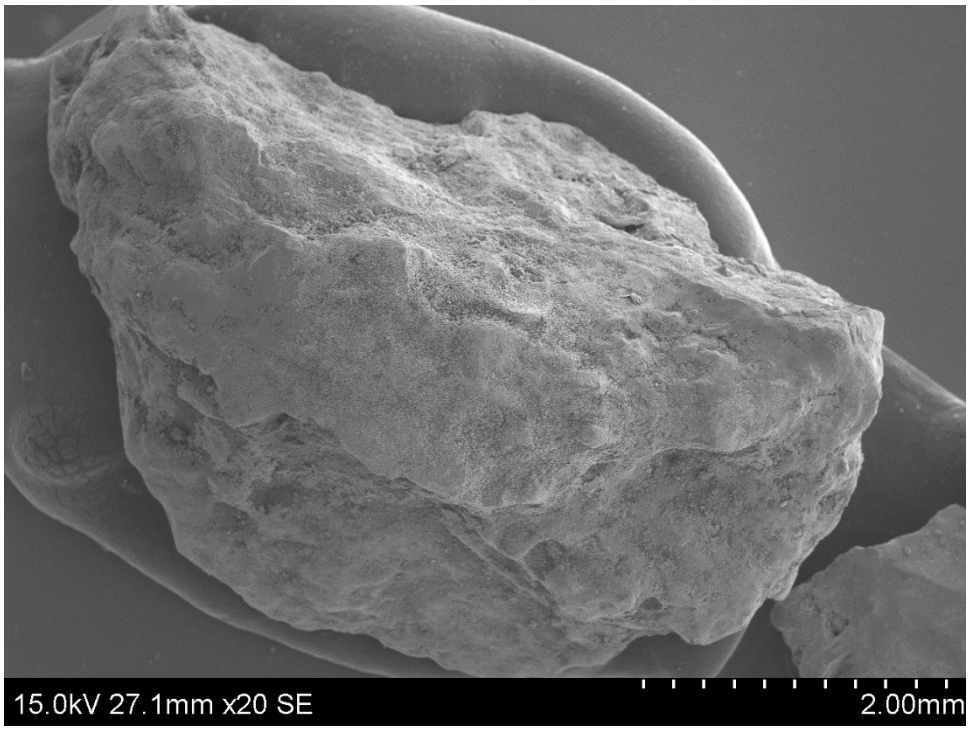

Figure 3 Scanning Electron Microscope (SEM) image of RCA05 (1.18-2.36 mm) fraction

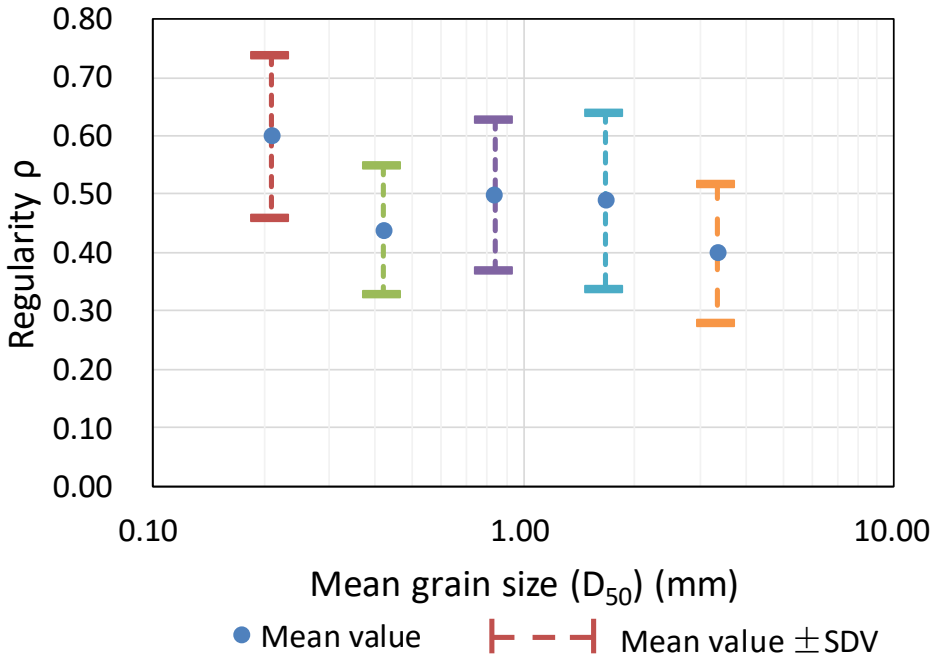

Figure 4 Particle shape regularity mean values ± one standard deviation (He and Senetakis, 2016a)

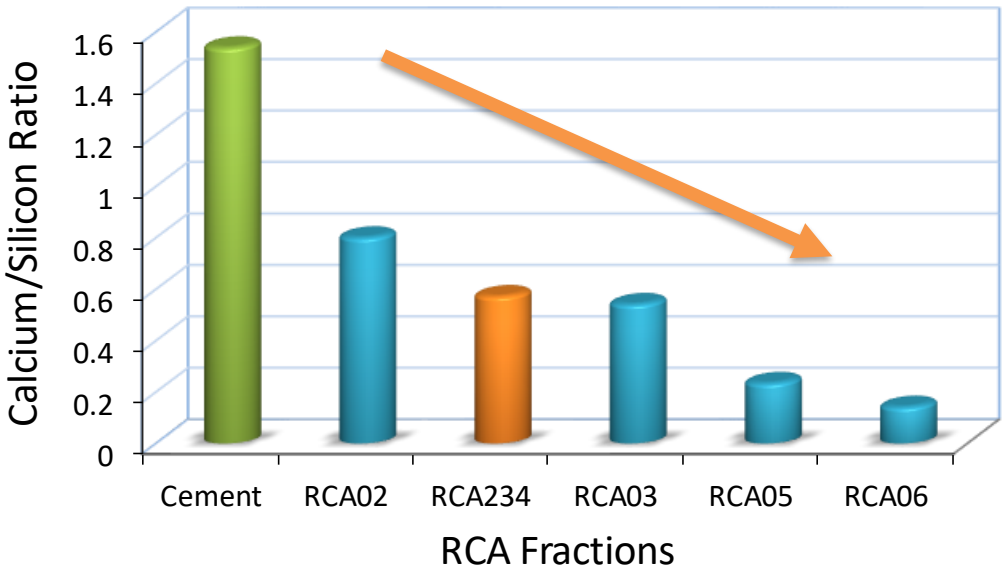

Figure 5 EDS testing results: Calcium to Silicon ratio for pure cement, different uniform fractions of RCA and one poorly graded RCA (updated after He and Senetakis, 2016a)

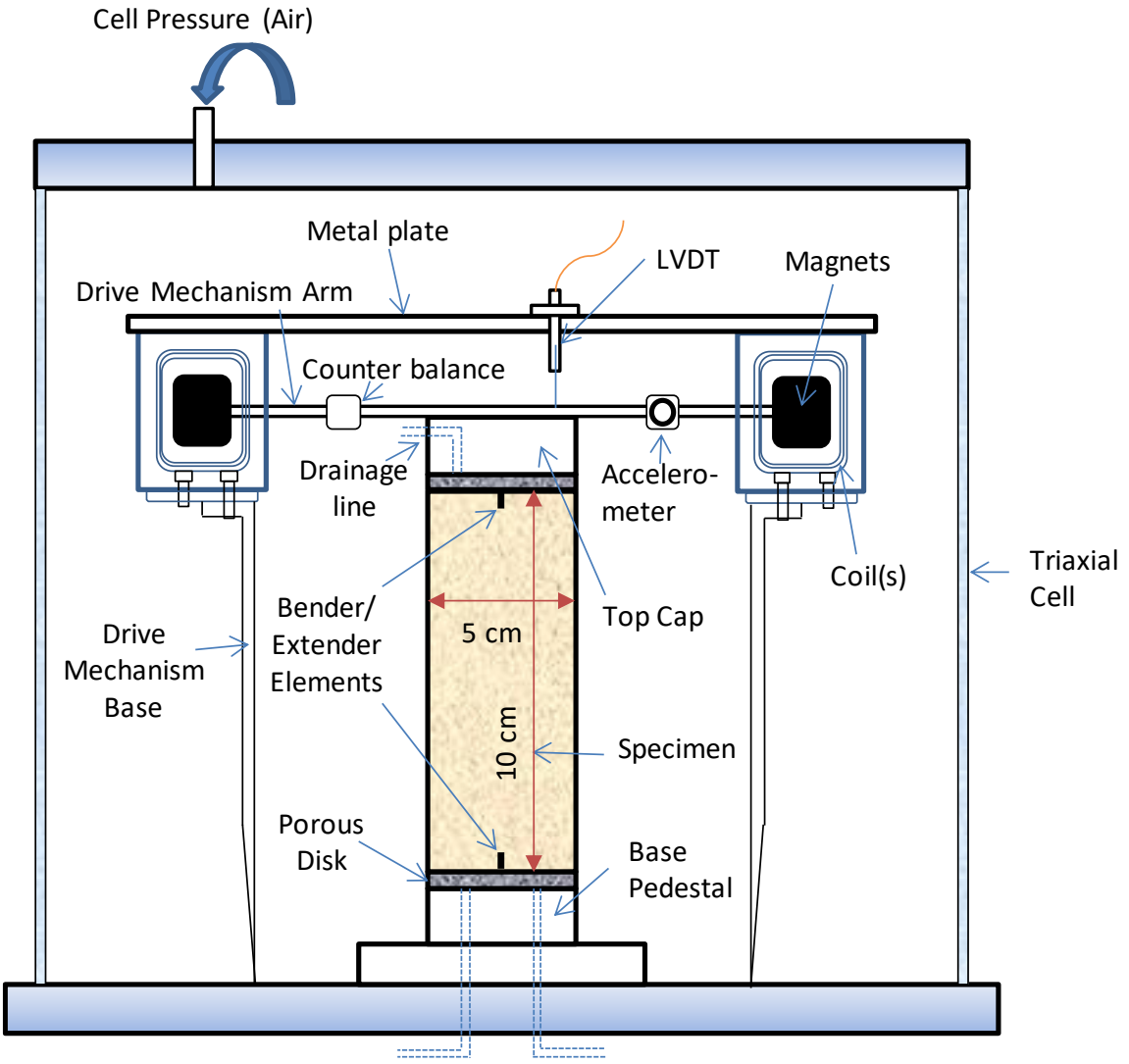

Figure 6 The schematic plot of the Stokoe-type resonant and the dimensions of the specimen

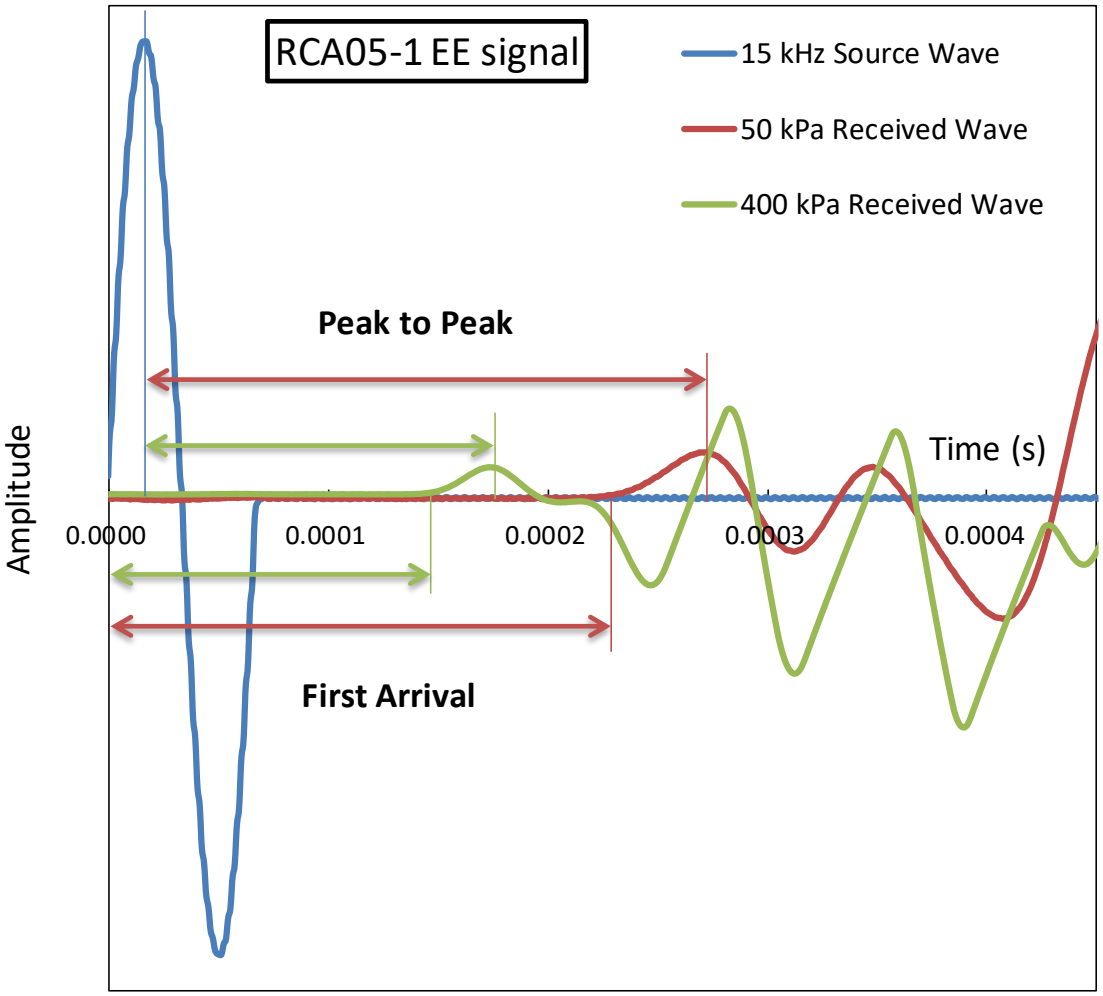

Figure 7 Example of the signal analysis methods for extender element test (specimen RCA05-1) Note: the amplitude for the source wave was at 14 V while the received wave was magnified 500 times to be discernable in the same plot

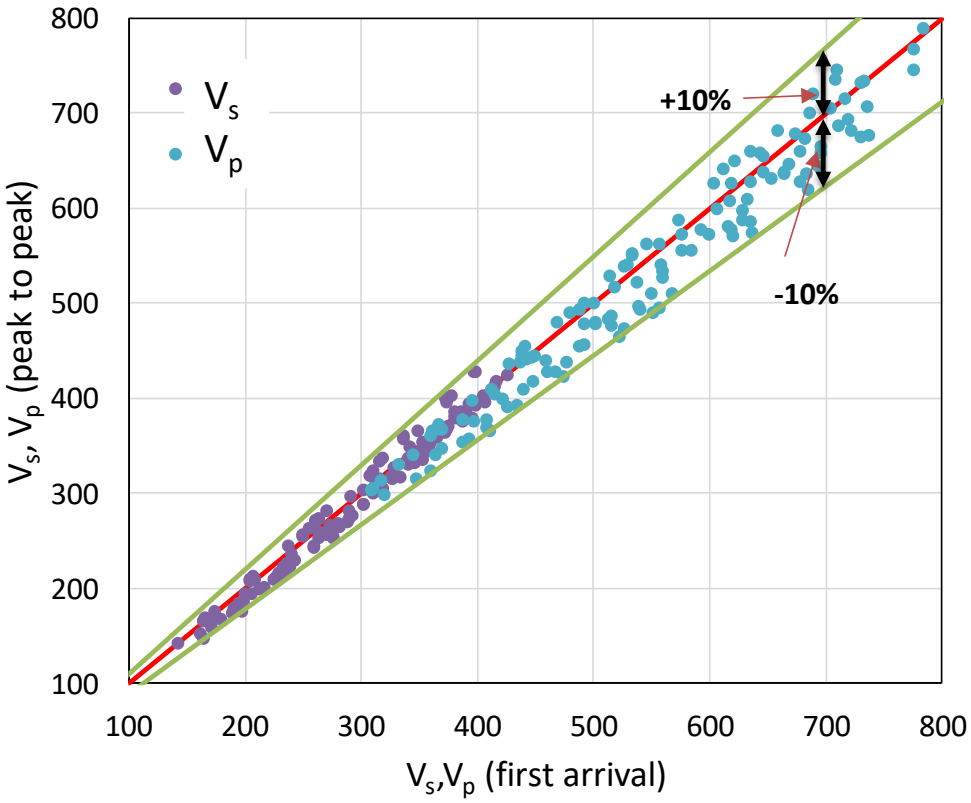

Figure 8 Comparison between wave velocities (V_s and V_p) results derived from first arrival and peak to peak methods during bender/extender element tests

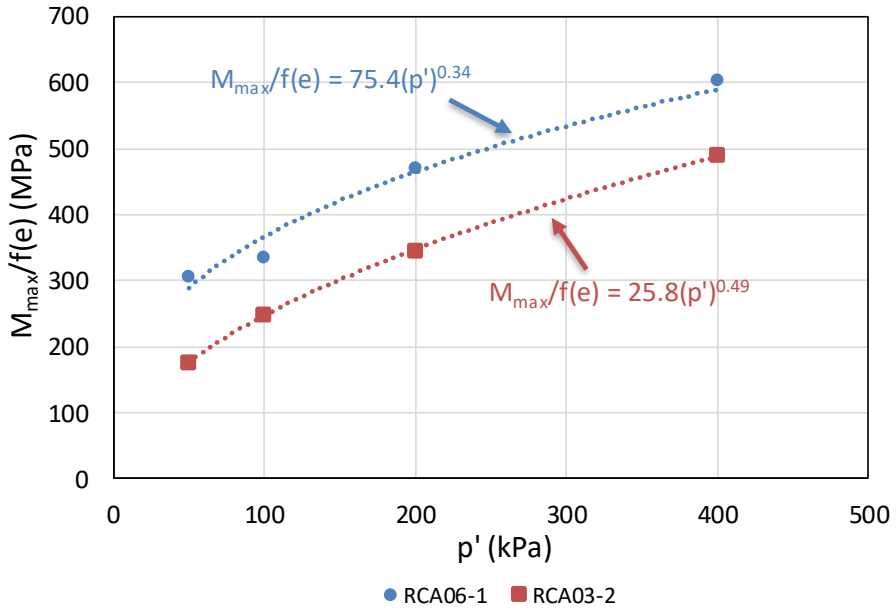

Figure 9 Typical plot of normalized constrained modulus (M_{max}) against mean effective stress (p') from two representative specimens: RCA06-1 and RCA03-2

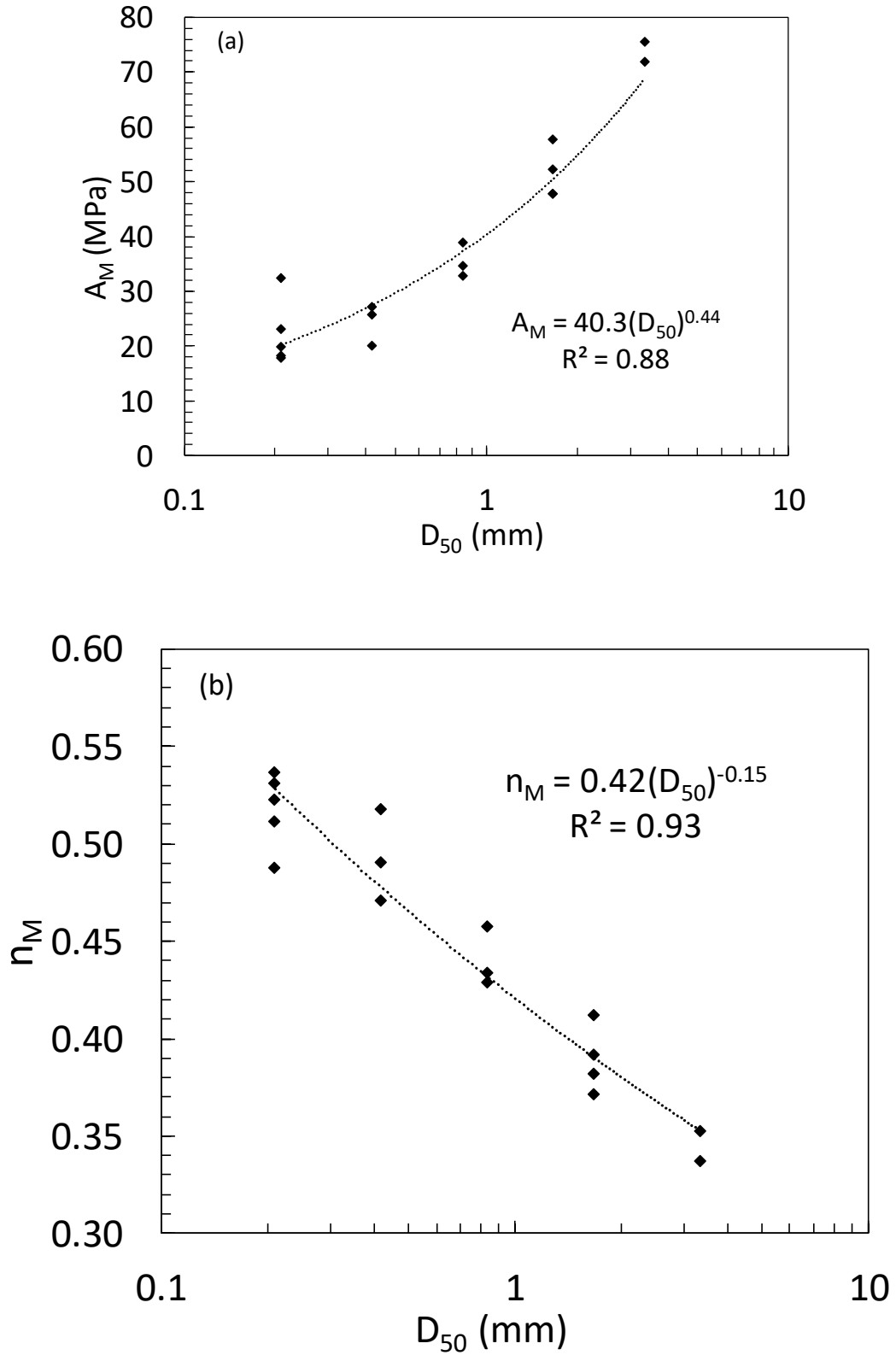

Figure 10 Illustration of the effect of mean grain size (D_{50}) on the small-strain constrained modulus constants: (a) Small-strain constant A_M and (b) Power n_M

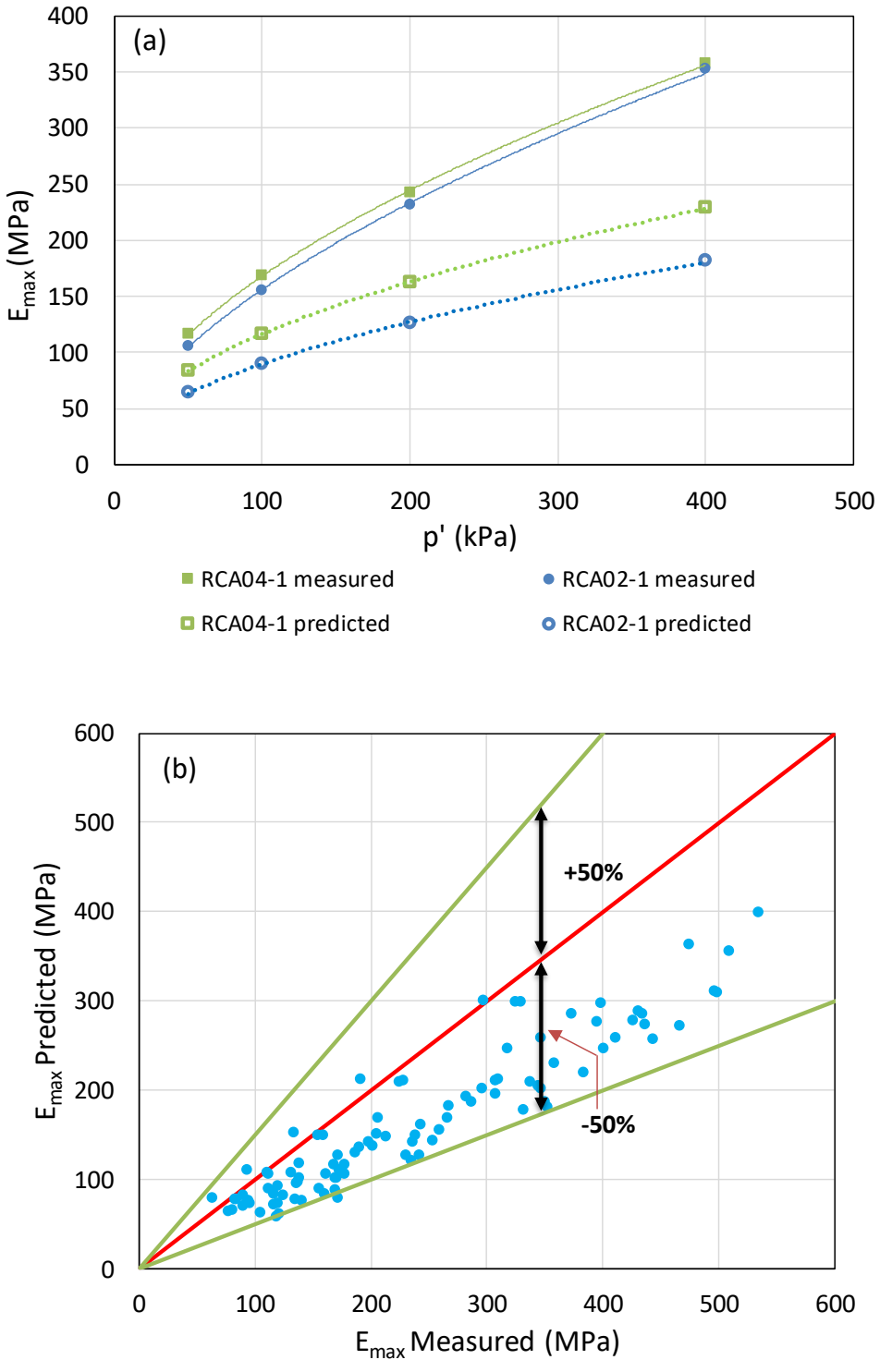

Figure 11 Comparison between predicted and measured small-strain Young's modulus values using the expression proposed by Payan et al. (2017): (a) measured E_{max} and predicted E_{max} against pressure from two representative tests; (b) all the measured and predicted Young's moduli

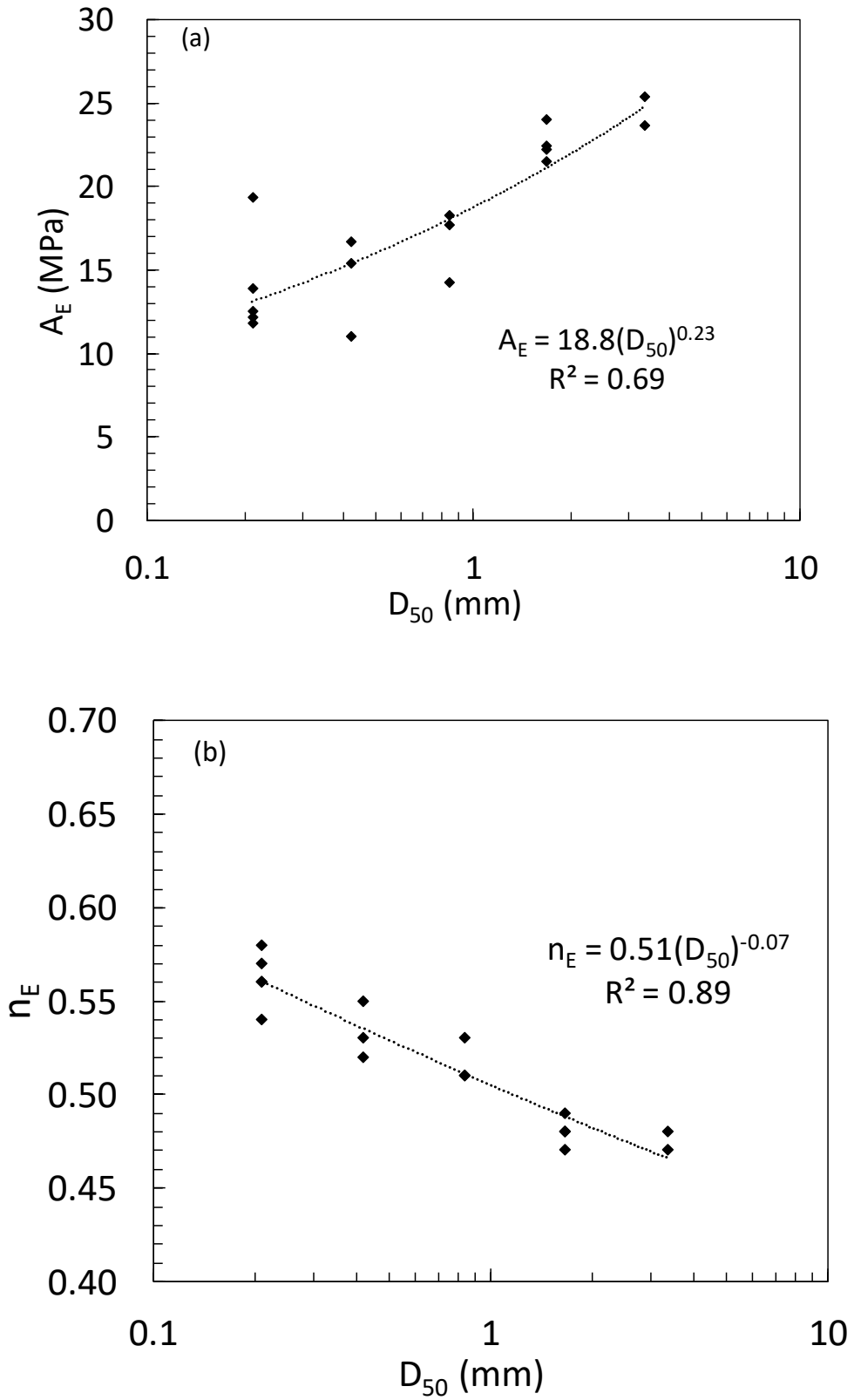

Figure 12 Illustration of the effect of mean grain size (D_{50}) on the small-strain Young's modulus constants: (a) Small-strain constants A_E versus D_{50} and (b) Power n_E against D_{50}

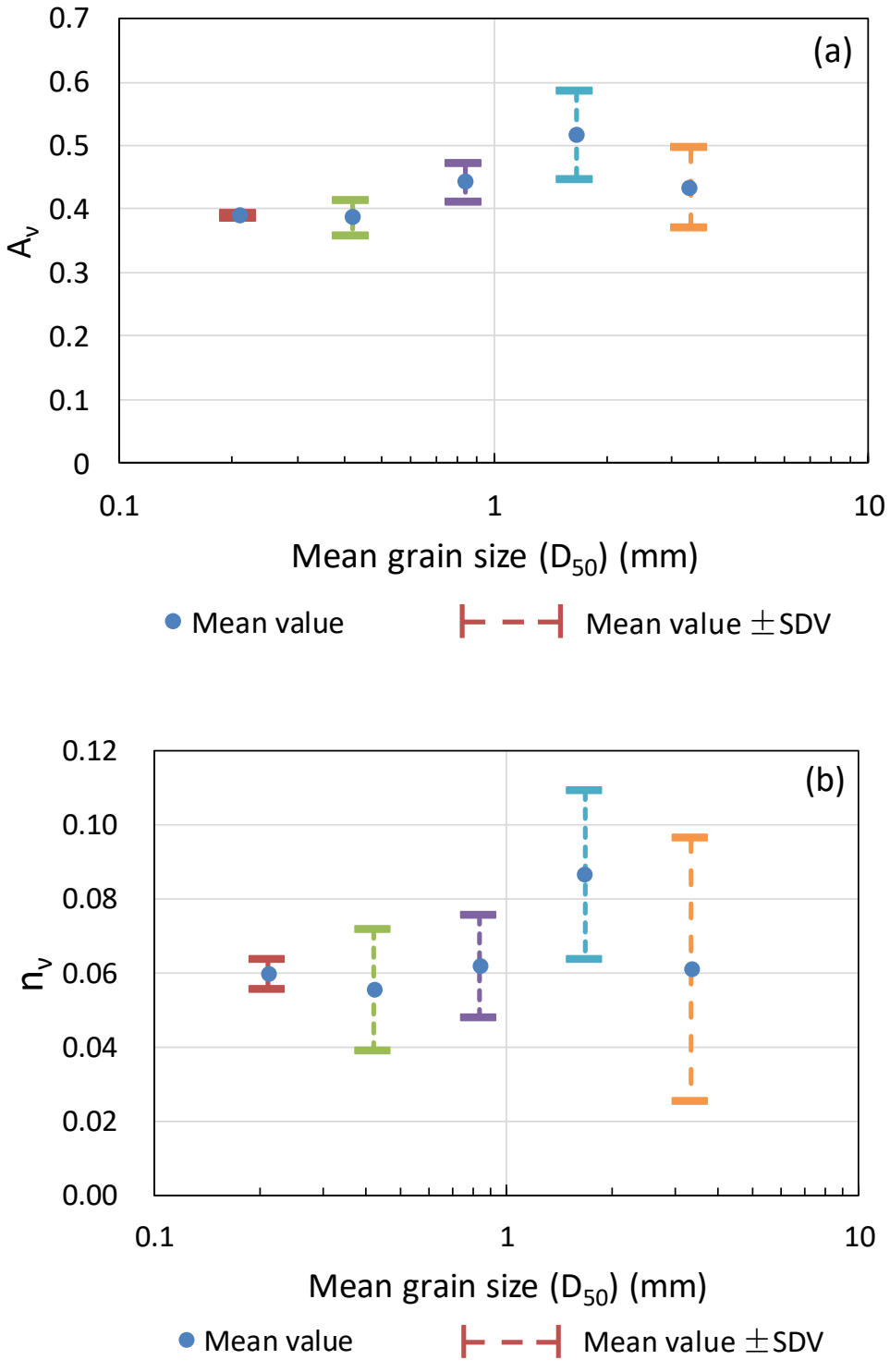

Figure 13 Illustration of the mean value ± one standard deviation for Poisson's ratio constants versus the mean grain size (D_{50}) from uniform fraction specimens: (a) Constants A_v versus D_{50} and (b) Power n_v against D_{50} (n_v are shown as absolute values)

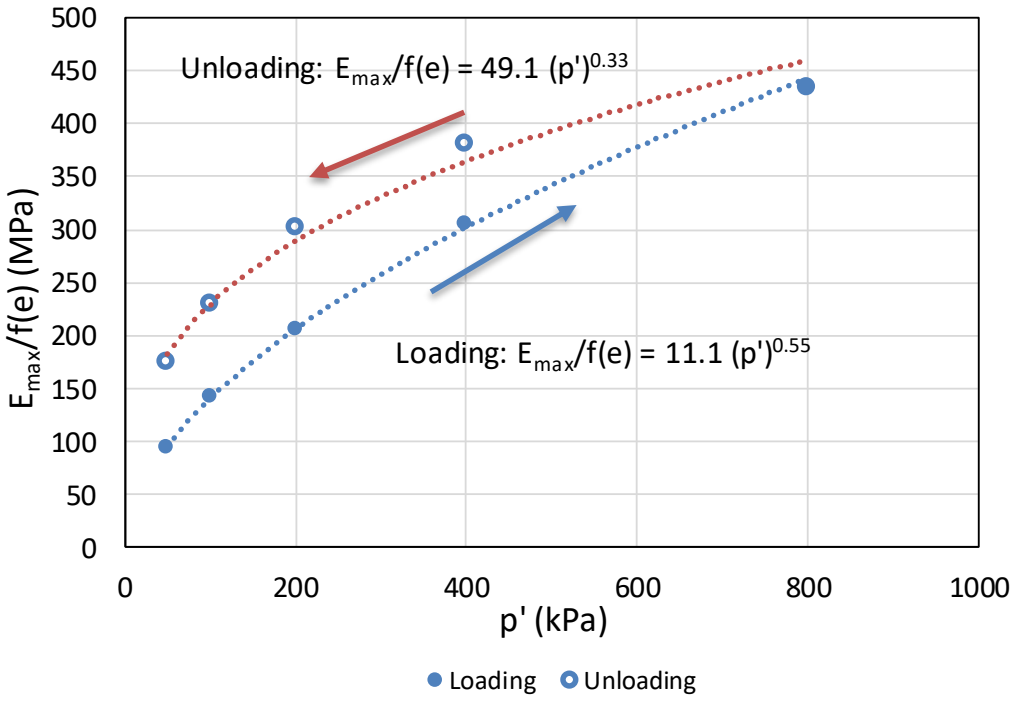

Figure 14 Loading and unloading behavior of normalized small-strain Young's modulus $E_{max}/f(e)$ against mean effective stress p' (from specimen RCA03-3)

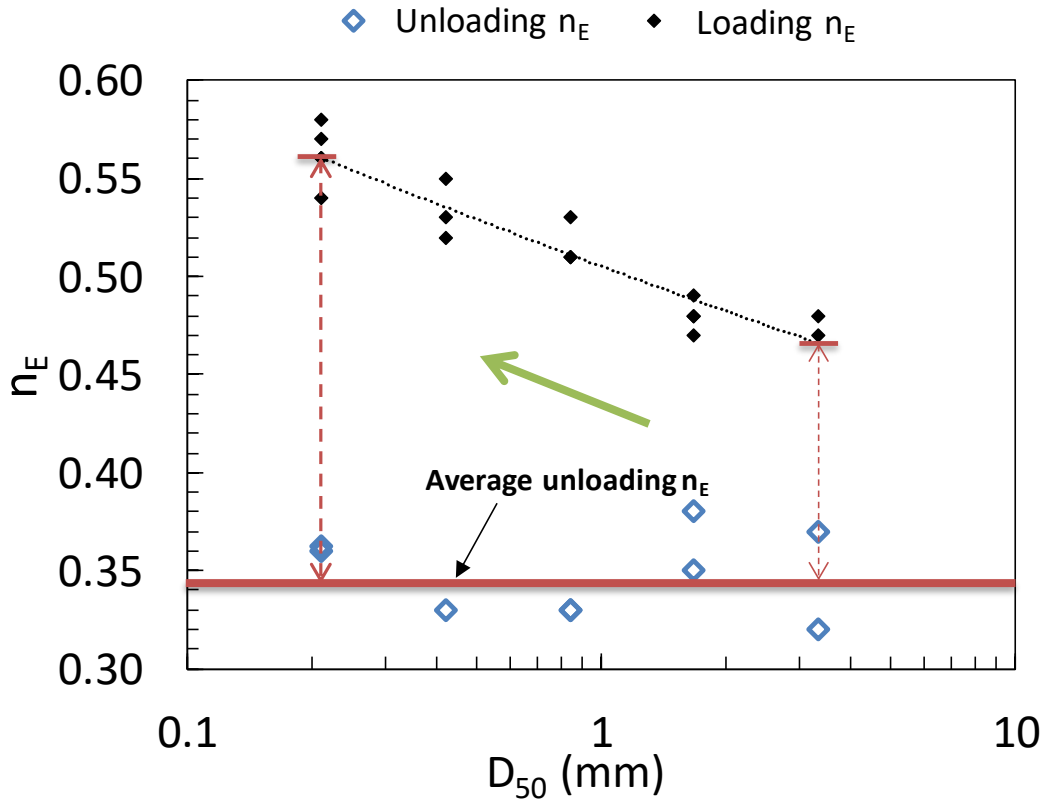

Figure 15 The comparison between loading and unloading power constant n_E

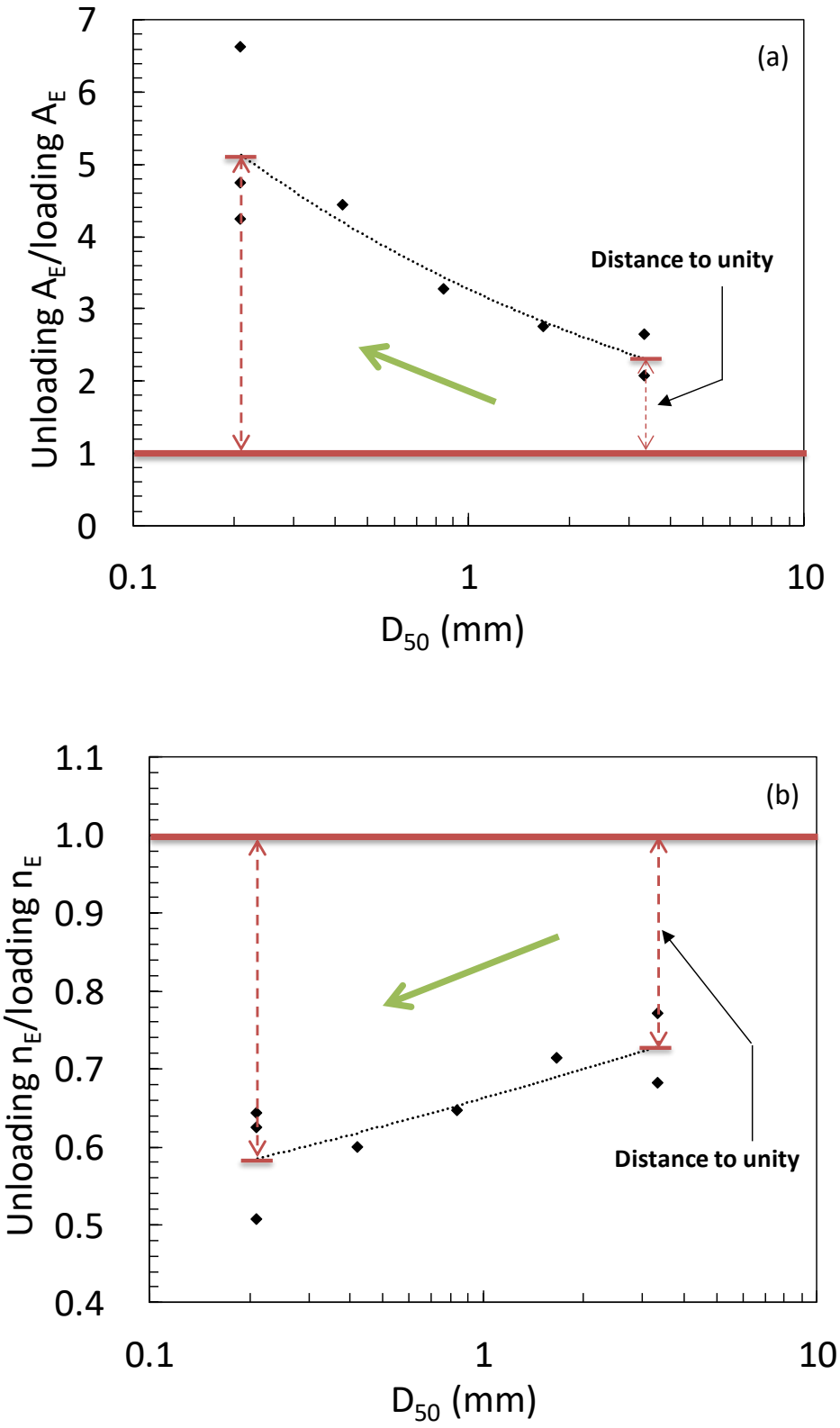

Figure 16 Unloading over loading small-strain Young's modulus constants versus mean grain size (D_{50}): (a) Unloading A_E/loading A_E against D_{50}; (b) Unloading n_E/loading n_E against D_{50}

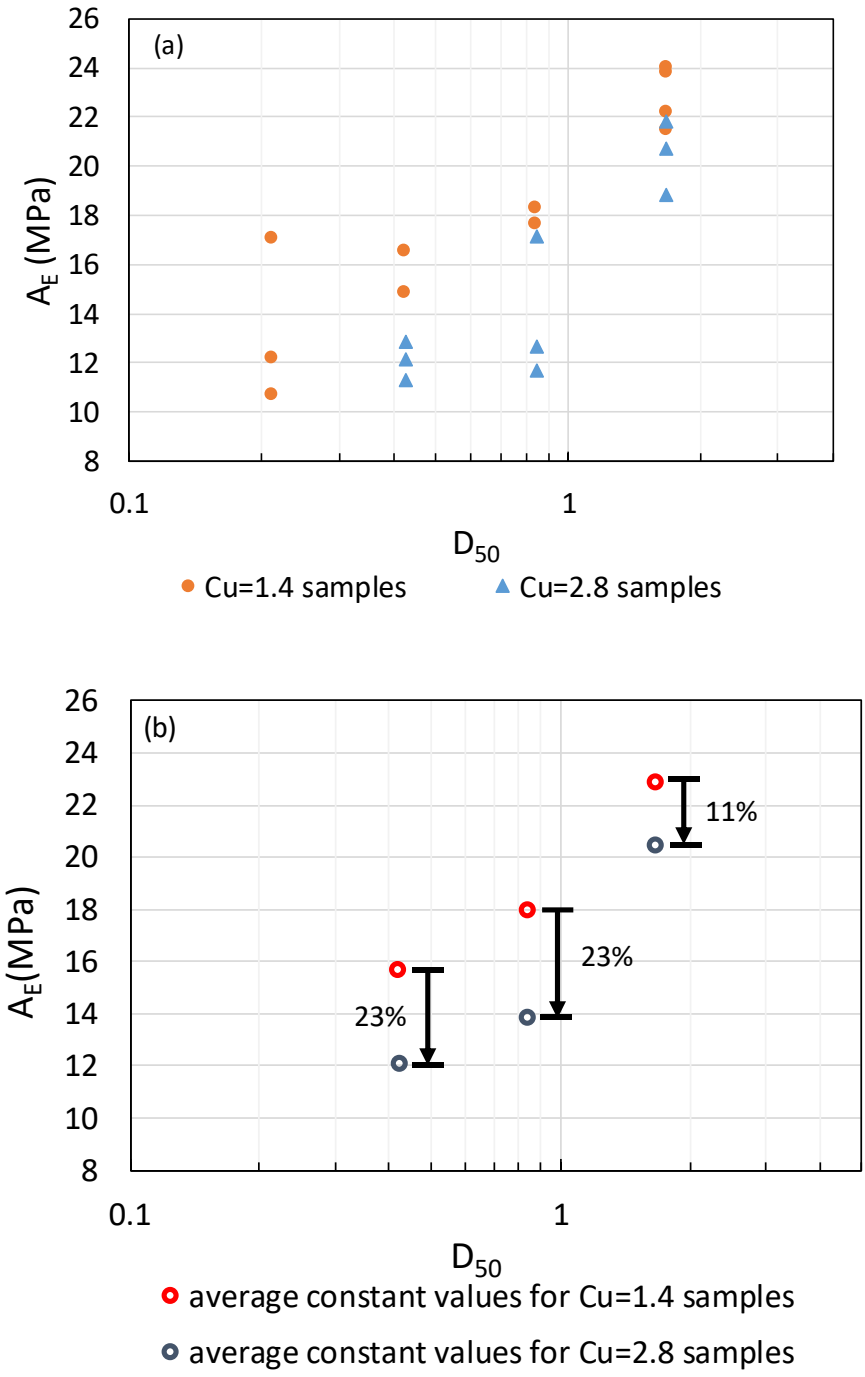

Figure 17 Comparisons of the effect of mean grain size (D_{50}) on the small-strain Young's modulus constants between well graded (C_u=2.8) and single fractions (C_u=1.4): (a) small-strain constants A_E versus D_{50} for each single test and (b) average A_E against D_{50}

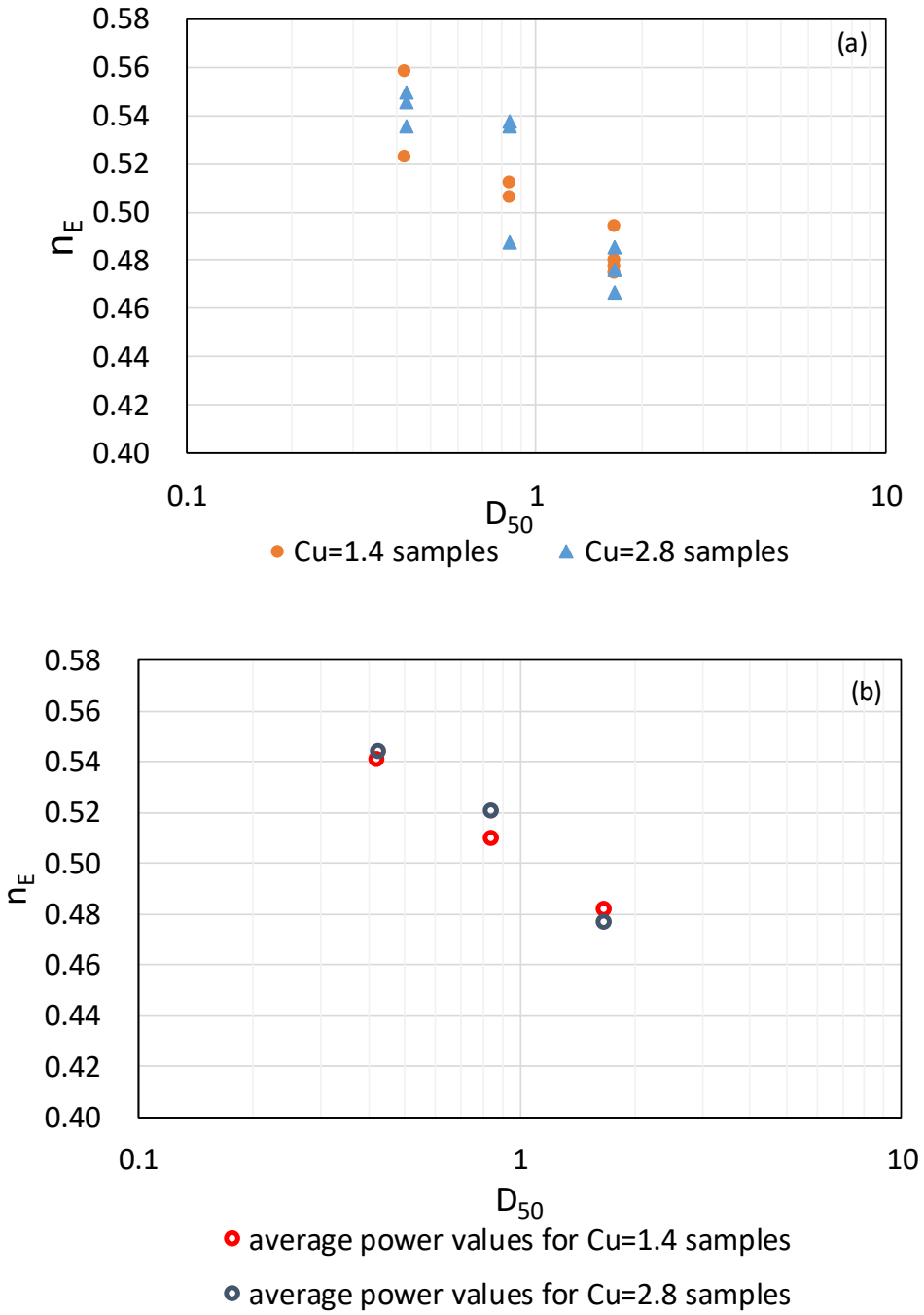

Figure 18 Comparisons of the effect of mean grain size (D_{50}) on the small-strain Young's modulus constants between well graded (C_u=2.8) and single fractions (C_u=1.4): (a) small-strain constants n_E versus D_{50} for each single test and (b) average n_E against D_{50}